Interaction Forces and Reversible Collapse of a Polymer Brush-Gated Nanopore

Roderick Y. H. Lim[†,*] and Jie Deng[‡]

[†]Biozentrum and the Swiss Nanoscience Institute, University of Basel, Klingelbergstrasse 70, Basel 4056, Switzerland, and [‡]Institute of Materials Research and Engineering, A*STAR (Agency for Science, Technology and Research), 3 Research Link, Singapore 117602

ABSTRACT Nanopores are ubiquitous in nature and technology, yet relatively little is known about how surface-grafted polymers can affect the interaction forces at the pore. By fabricating Au nanorings on Si substrates, we have constructed a unique experimental platform that allows for direct atomic force microscope (AFM) measurements to be made on polyethylene glycol (PEG) chains locally anchored onto a geometric pore surface. Force measurements show that the PEG gives rise to a steric repulsive barrier that envelops the entire nanoring, signifying polymer brush formation. This is confirmed by a direct imaging of the PEG brush, which reversibly collapses by switching between poor and good solvent conditions to "open" and "close" the pore, respectively. From the view of interaction forces, these results highlight possible functionalities in which polymer brushes may play a role in minimizing fouling/clogging effects in synthetic nanopores and biological nuclear pore complexes (NPCs). By the mechanism of a reversible collapse, this work illustrates how polymer brush-gated nanopores may be used as nonfouling sieves for small molecules and/or solvent-controlled chemical valves that regulate solute traffic.

KEYWORDS: polyethylene glycol · molecular gating · polymer brush · reversible collapse · steric repulsion · fouling · nanofabrication · force volume spectroscopy

Polymers at surfaces regulate interfacial phenomena in diverse areas ranging from tribology to colloidal stability and biology.[1] In biomedical and biotechnological applications, for instance, polypeptide drugs and nanoparticles designed for drug delivery[2] exhibit enhanced biocompatibility and protein resistance (*e.g.*, "stealth" particles)[3] when modified with polymers such as polyethylene glycol (PEG), that is, PEGylation.[4] On the basis of its low toxicity, PEG is also widely used as a protein-resistant surface coating.[5−7] Surface-grafted (bio)polymers are also widely used in ultrafiltration membranes for water purification,[8] as chemically gated valves for permeation control,[9−12] and as synthetic mimics of biological nanopores.[13,14]

While such examples underscore their technological impact on society, a comprehensive understanding of the fundamental properties of surface polymers is perhaps still lacking.[1] To a large extent, this uncertainty stems from limitations in instrumental and experimental design. The surface force apparatus, which has contributed immensely to our understanding of intermolecular and surface forces,[15] uses a cross-cylindrical setup and is limited to a contact area of $\sim 10^{-5}$ cm^2. The atomic force microscope (AFM) may have the added advantage of using an ultrasharp tip typically with a radius of curvature of ~10 nm, yet most AFM studies of interfacial forces have been focused on flat substrate surfaces.[16] Today, the influx of applications employing nanoparticles and nanopores calls for directed attention to be paid to the local properties and forces of surface polymers on nanoscale objects exhibiting complex geometries and architectures.[17−23]

A specific case that has not been comprehensively addressed concerns the behavior of polymer chains tethered to a nanopore. Despite having wide technological appeal, fundamental studies targeting such behavior have been largely restricted to theoretical modeling and simulations.[24,25] Much less is known about how polymers tethered around the entrance of a nanopore can influence the interaction forces on an approaching object and how this would affect its likelihood to enter into the nanopore. Clearly, the presence of polymers can significantly affect nanofluidic pore functionality due to the large surface-to-volume ratio at such molecular length scales.[26] Thus, any information regarding such local effects can prove useful toward improving membrane design such as to minimize nonspecific material accumulation and clogging (*i.e.*, fouling).[26−28]

The driving impetus behind our current work stems from a desire to understand the underlying physical basis of how

*Address correspondence to roderick.lim@unibas.ch.

Received for review February 15, 2009 and accepted August 21, 2009.

Published online September 3, 2009. 10.1021/nn900152m CCC: $40.75

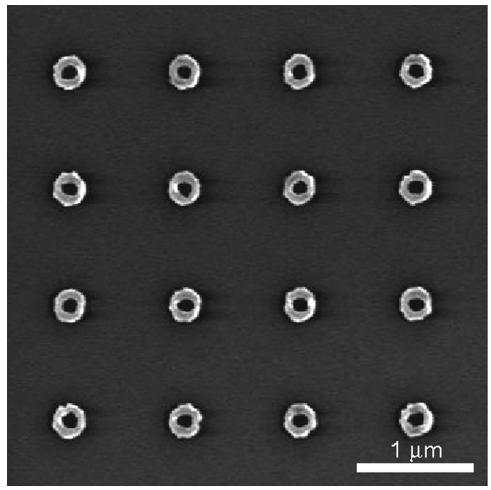

Figure 1. Arrays of Au nanorings measuring 34.0 ± 1.6, 87.1 ± 9.6, and 213.3 ± 8.3 nm in height (AFM), inner and outer diameters (SEM), respectively, have been nanofabricated on Si substrates. Scale bar, 1 μm.

surface-tethered polymers can influence the interaction forces and morphology at a nanopore. Here, we have exploited nanofabrication technology as a means to construct toroidal nanostructures exhibiting geometric pore surfaces (*i.e.*, Au nanorings). This provides us with the unique opportunity to study the behavior of tethered polymers beyond ideal surfaces (*e.g.*, flat planes and spheres). By covalently tethering PEG chains to the Au nanorings, we have investigated the corresponding interaction forces and morphology of the PEG chains surrounding the nanoring at the solid−liquid interface using a combination of AFM force measurements and imaging. Importantly, our choice of PEG is governed by its biocompatible, nonfouling properties[7] (*i.e.*, resistance to protein adsorption). When confined by the AFM tip, the PEG chains give rise to an exponentially decaying long-ranged repulsive force that is characteristic of a polymer brush (*i.e.*, steric repulsion). This force is detectable over the entire nanoring, indicating that the PEG collectively forms a repulsive barrier that extends over the pore entrance even though the PEG chains are not directly tethered at the base of the pore. Further analysis of our measurements reveals that the interaction stiffness at the pore entrance is quantitatively less than what is measured along the surface of the nanoring. This observation is confirmed in AFM images, which provide a direct visualization of the polymer brush barrier. By increasing the scanning force, the AFM tip appears to progressively splay or penetrate the brush to reveal the underlying nanoring structure. The brush covers the central pore once the scanning force is reduced. Finally, by switching between poor and good solvent conditions, we demonstrate how the reversible collapse of PEG chains can effectively act as a gate to "open" and "close" the pore.

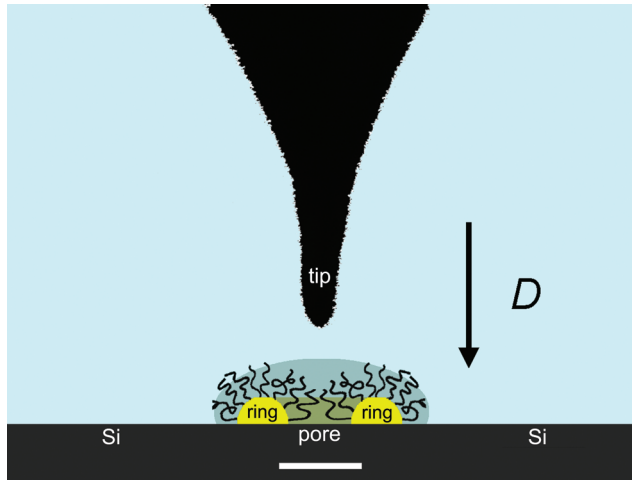

Figure 2. To-scale schematic description of the AFM experiment. The outline of the AFM tip (R_{tip} = 16.1 ± 2.4 nm) is taken directly from its corresponding SEM image (acquired after the experiment) and blackened. The opening angle at the very end of the tip is ~8°. The bare Si area surrounding the nanoring, the ring surface, and the pore are defined as in the text. *D* is defined as the tip−sample approach distance. The gray shaded area demarcates the range of the PEG chains that extends beyond the periphery of the Au nanoring. Scale bar, 100 nm.

RESULTS

Figure 1 shows a scanning electron microscope (SEM) image of the Au nanoring array on a Si substrate, which was generated by electron-beam lithography (see Methods). We used a "grafting to" technique[29] to covalently anchor thiol-terminated 20 kDa PEG chains (mPEG-thiol) onto the Au nanoring surfaces from solution (see Methods). The hydrodynamic diameter of the 20 kDa mPEG-SH is measured to be 8.6 ± 1.8 nm by dynamic light scattering with a polydispersity index (PDI) value of 0.075 (*i.e.*, monodisperse; see Methods; data not shown). Each nanoring is spaced 1 μm apart to ensure that, after binding to the Au, individual clusters of PEG remain physically isolated from each other. The lateral dimensions of each nanoring as determined by SEM are 87.1 ± 9.6 and 213.3 ± 8.3 nm for the inner and outer diameters, respectively. These dimensions are reproduced within error when measured by AFM, from which we find the inner and outer diameters to be 80.1 ± 4.4 and 205.9 ± 9.9 nm, respectively, with a nanoring height of 34.0 ± 1.6 nm.

To study the interaction forces at each nanoring, arrays of AFM force measurements were acquired in force-volume (FV) mode, which provides a spatial map of individual forces at specific topographic locations (X, Y). As defined in Figure 2, these locations can be grouped into (i) the bare Si area surrounding the nanoring (henceforth termed Si), (ii) the upper Au surface of the nanoring (henceforth termed ring), and (iii) the central pore (henceforth termed pore).

Specifically, Figure 2 represents a to-scale schematic description of an experiment conducted using a cantilever of spring constant, $k_C \approx 0.006$ N/m, and a tip with a radius of curvature (R_{tip}) of 16.1 ± 2.4 nm (determined by SEM after AFM experimentation). The data we report in this paper are representative AFM force

profiles obtained with this tip. Experiments with different tips were found to exhibit qualitatively similar force profiles with varying magnitude, which we attribute to quantitative differences in tip roughness and geometry. On the basis of the dimensions shown, complete penetration into the pore is possible due to the small tip size (compared to the pore diameter). Moreover, the small opening angle at the very end of the tip (~8°) ensures that tip artifacts are minimized during imaging, as evidenced in the comparable nanoring dimensions obtained by both AFM and SEM.

Experiments conducted in phosphate buffered saline (PBS) show that distinct force curves are distinguishable in each of the three general locations (*i.e.*, Si, ring, and pore) (Figure 3A). For each force curve, we have assigned $D = 0$ (where D is the tip−sample approach distance; see Methods) to the region where the force increases infinitely (*i.e.*, hardwall repulsion). It must be noted, however, that we cannot be certain if the PEG chains are laterally displaced or under further compression by the tip at $D = 0$. In the Si area, the lack of any detectable long-range repulsion results from the screening of the electrostatic double layer at the present buffer conditions (PBS Debye length = 0.76 nm).[30] At the ring, the force is repulsive with a detectable onset at a separation distance of $D \sim 35$ nm above the Au surface. Although an exact point of contact is difficult to establish, this is the distance where the approaching tip sufficiently compresses the PEG brush to elicit an exponentially decaying, long-range repulsive force (*i.e.*, steric repulsion) which causes the cantilever to deflect. Accordingly, as described by the Alexander−de Gennes (AdG) theory,[31−33] the compressive response of a polymer brush measured by the AFM tip over the restricted range $0.2 < D/l < 0.9$ can be approximated by[34,35]

$$\frac{F(D)}{R_{tip}} = \frac{100\pi D}{s^3} k_B T e^{-2\pi D/l} \qquad (1)$$

where k_B is Boltzmann's constant, T is the absolute temperature, F is the measured force (as a function of D), s is the average distance between anchor sites, and l is the effective brush height (see Supporting Information). Equation 1 adequately describes the measured steric repulsion in the limit where D is less than l (*i.e.*, $D/l <$ 0.9). The lower limit in the approximation essentially ignores the strong osmotic repulsive forces of the chains at $D/l < 0.2$. Because s depends on the site of tip interaction with respect to the toroidal geometry of the nanoring (not defined in this approximation), we have limited our analysis to l (where s has no consequence on the exponential decay length) and find that eq 1 provides for an appropriate fit to the ring force data from which we obtain $l_{ring} = 38.9 \pm 4.4$ nm as the height of the brush above the ring (Figure 3A inset).

Interestingly, the force measured directly at the pore entrance is also long-ranged and sterically repul-

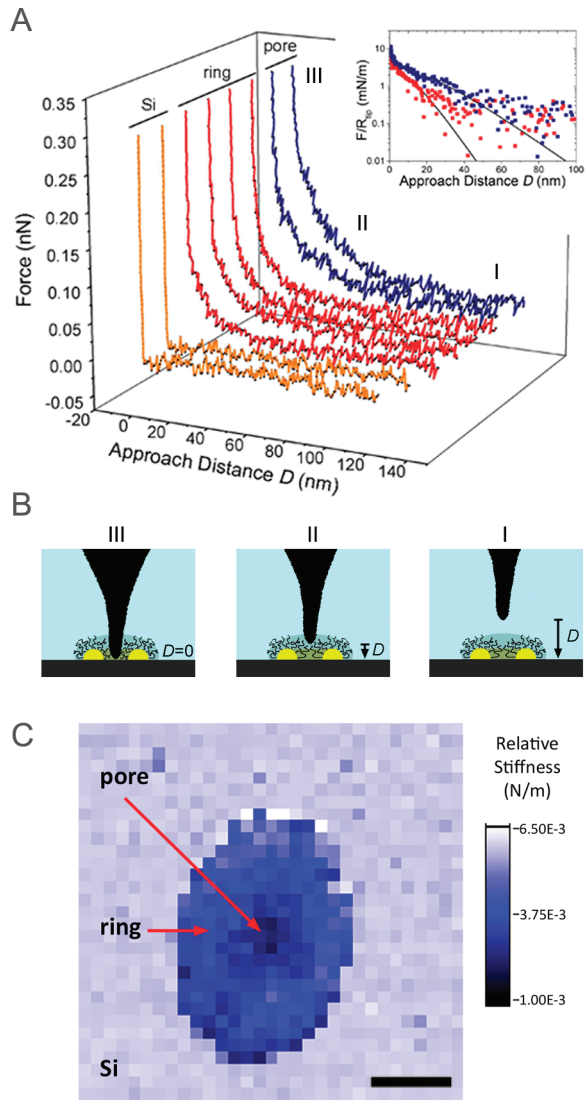

Figure 3. Representative force curves of a PEG-gated nanoring obtained in FV mode. (A) Force measurements are distinguishable over three distinct locations: (i) the pore (blue), (ii) the surface of the ring (red), and (iii) the surrounding Si surface (orange). Both the pore and the ring exhibit forces that are long-ranged and sterically repulsive, originating at $D \sim 70$ nm away from basal Si surface of the pore and $D \sim 35$ nm away from the ring surface, respectively. The force in the surrounding area is negligible until the tip comes into hardwall contact with the Si surface. Inset: AdG fits (black lines) from which we obtain brush heights of $l_{pore} = 71.0 \pm 4.6$ nm and $l_{ring} = 38.9 \pm 4.4$ nm at the pore (blue) and ring (red), respectively. By subtracting the height of the ring (34 nm) from l_{pore}, we find that the steric repulsion above the pore commences at a distance of ~37 nm above the ring surface. This is in agreement with the value of l_{ring} and indicates that the steric repulsion has a consistent vertical range that envelops the entire nanoring (as drawn in Figure 2; see text for details). The data collected beyond a certain D are scattered because it is less than the minimum detectable force, which is given by the thermal noise of the cantilever: $F_{min} = (k_B T \times k_c)^{1/2} = 5$ pN. This equates to a F/R_{tip} value of 0.3 mN/m. (B) Schematic description of the tip−brush interaction at the pore as measured in (A). I: At large D, the tip is not in contact with the PEG brush and no repulsion is detected. II: The tip gradually compresses the brush at the pore opening, which gives rise to a repulsive force as described in the text. III: Hardwall contact is made where D remains at zero despite any further increase in the force. (C) Corresponding FV stiffness map showing the spatial distribution of the steric repulsion. The relative stiffness (color coded in the scale bar) shows that the steric repulsion is localized at the nanoring and that the pore has the lowest interaction stiffness. Scale bar, 100 nm.

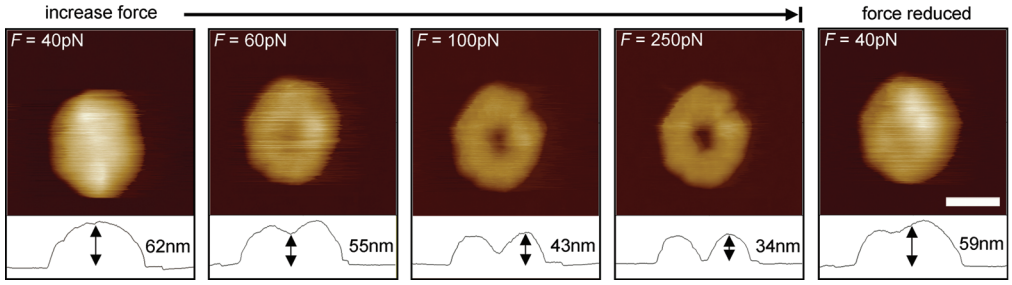

Figure 4. Visualizing the polymer brush-gated steric barrier. The first four panels illustrate the effect of increasing the force set point during contact AFM imaging. At low force (40 pN), the pore is completely obscured by the PEG brush with an overall height of 62 nm (*i.e.*, the steric repulsive barrier). As the force is increased from 40 to 60 to 100 pN, the AFM tip gradually compresses/displaces the PEG brush to reveal the underlying nanoring and, in particular, the central pore. At 250 pN, the height of the ring is 34 nm, which indicates that the tip has completely penetrated/splayed the PEG brush. The fifth panel shows that the central pore becomes covered again after the force set point is reduced back to 40 pN. Scale bar, 100 nm.

sive even though the PEG chains are not tethered to the pore's basal Si surface but limited to the inner walls and surface of the ring. Here, the steric repulsion commences at about $D \sim 70$ nm away from the hardwall contact (Figure 3A; from eq 1, the pore brush height, $l_{pore} = 71.0 \pm 4.6$ nm). As shown in Figure 3B, the tip has to traverse through the pore (*i.e.*, the pore depth equals the ring thickness) before coming into hardwall contact with the basal Si surface. By subtracting the height of the ring (34 nm) from l_{pore}, we find that the steric repulsion above the pore also commences at a distance of ~37 nm above the ring surface. This is in agreement with the value of l_{ring} and indicates that the steric repulsion has a consistent vertical range that envelops the entire nanoring.

A qualitative view of the in-plane force distribution can be resolved in the corresponding FV stiffness map (Figure 3C), which is generated by calculating the relative stiffness of each measurement within a force range of 0.05 and 0.15 nN (see Methods for a detailed description). Observe that the steric repulsive zone is strictly localized to the nanoring (*i.e.*, ring and pore), which gives rise to a lower relative stiffness (dark). This is markedly different as compared to the surrounding Si area (bright), which has a relative stiffness equaling the spring constant of the cantilever ($k_C \approx 0.006$ N/m) and indicates that the tip is in hardwall contact with the Si surface. It is apparent from the darkest region (stiffness ≈ 0.001 N/m) that the PEG brush can still form a steric repulsive barrier at the pore. This also confirms that the forces above the nanoring do not originate from the nonspecific aggregation (or contamination) of material at the AFM tip. It is imperative to find that the large variation in the relative stiffness is not reproduced in control experiments performed in the absence of PEG. In such cases, hardwall contact is observed at all locations (data not shown).

Generally, the magnitude of F scales with the size of an approaching object (R).[15] Therefore, the steric repulsion exerted on an oncoming particle (modeled by the AFM tip in the present case) should effectively prevent it from entering the pore. To demonstrate such an effect, AFM images of the PEG brush have been acquired by varying the contact imaging force in accordance with the known steric repulsion (Figure 3A). Having prior quantitative knowledge of the resulting steric repulsion, the underlying nanoring remains unresolved at low scanning forces ($F =$ 40 pN) because the scanning tip does not effectively displace the PEG brush (Figure 4). Instead, we observe an overall barrier-like morphology with a maximum cross-sectional height of 62 nm corresponding to l_{pore} (with respect to a low scanning force of ~40 pN). Only by increasing the force from 40 to 60 to 100 pN is the underlying nanoring structure gradually resolved due to the compression or penetration/splaying of the PEG chains by the AFM tip. By examining the cross-sectional profile of each image, we find that the PEG chains are most easily deformed at the pore as compared to the ring, which is in agreement with the low stiffness of the PEG brush there (Figure 3C). At high scanning forces ($F = 250$ pN), the AFM tip completely displaces the PEG and finally detects the base of the central pore as well as the ring height (*i.e.*, 34 nm). Importantly, the PEG brush covers the pore again once the force is reduced to 40 pN.

Poor solvents are anticipated to produce a significant change in surface polymers (*i.e.*, collapse), thereby inducing an opening of the pore.[24,25] To demonstrate how such a collapse can promote the selective opening of the pore, we have added 10% 2-propanol (a poor solvent for PEG)[36] to the buffer conditions and observe that the PEG chains are no longer in an extended polymer brush conformation (Figure 5A). Using a low scanning force of ~40 pN as above, we observe that the PEG chains have collapsed toward their anchoring sites to form compact globules on the surface of the ring. This observation is consistent with the collapse of a thiol-terminated polystyrene brush in poor solvent conditions (so-called pinned micelles),[37] although we cannot be certain if the scanning AFM tip exerts any influence over the quantitative extent of the collapse. In the absence of the polymer brush barrier, the pore is now in an "open" state. Notably, the collapse is reversible by re-establishing the original buffer conditions. This returns the PEG chains into their barrier-like, polymer brush conformation resulting in a "closed" pore as before (Figure 5B).

DISCUSSION

Polymer brush formation occurs when the lateral distance between the anchoring sites of neighboring polymer chains is close enough to cause the chains to overlap and distend with a net directionality away from the anchoring surface in good solvent conditions.[31,32,38,39] Otherwise, polymer chains anchored far apart from each other retain their approximate hydrodynamic diameter to form "mushrooms" at low surface densities.[15,31,32] In the present study, both AFM images and force measurements indicate that the PEG chains exhibit a preferred perpendicular orientation with respect to the nanoring surface. On the ring, the PEG extension is almost 5 times (~40 nm) its hydrodynamic diameter of 8.6 ± 1.8 nm, but not exceeding its contour length estimated by $L_C = a \times n = 126$ nm, where a is the mean monomer length in water (2.8 Å)[40] and n is the number of repeat units within the PEG chain ($n \simeq 450$). This is in general agreement with previous force studies of planar PEG brushes.[7,30,41] Nevertheless, the unperturbed brush height may be underestimated in our experiments because the technique is insensitive to tip-induced changes in the PEG chains that occur below the AFM force resolution.[42]

It is noteworthy that an exponentially decaying, long-range steric repulsive force is detected at the pore. As opposed to simply "coalescing" or residing within the pore interior, this suggests that the PEG chains tethered close to and around the pore walls overlap in a radial orientation and extend to a large extent out of the pore (Figure 5B). Similar effects have been observed where polymer brushes grafted onto neighboring nanostructures tend to overlap once the distance between their grafting regions is small enough.[22,43] Variations in topography and surface density are likely to cause intrinsic differences in the local brush structure on the ring and at the pore. Generally, we find that (i) the repulsion at the pore reaches a higher force before the hard contact regime is reached (Figure 3A), and (ii) the relative stiffness at the pore is smaller than that at the ring surface (Figure 3C). A plausible explanation for the lower stiffness may be that the overall chain density is lower in the pore interior (recall that the PEG is not tethered at its base). On the other hand, a higher force is required to reach hard contact because the PEG chains end up being "trapped" and strongly compressed inside the pore by the confining tip.

From a strict interaction forces perspective, the current measurements show how a polymer brush can act as a repulsive barrier at the entrance of a nanopore. Importantly, eq 1 establishes that the magnitude of F scales with the size of the approaching particle (R) and reveals how the effectiveness (*i.e.*, range and magnitude) of the brush barrier increases for larger particles and objects. Small molecules such as water and ions would more easily diffuse through such a barrier (*i.e.*, the brush consists of hydrated PEG chains). While this conjecture remains to be validated using legitimate transport measurements through freestanding nanopores (*e.g.*, as a function of pore depth/size, PEG chain length, *etc.*), there is evidence in the literature showing that polymer brush formation does play a role in the nonfouling properties of PEG-modified ultrafiltration membranes.[44] (Note: A caveat that is not considered in the interpretation of our results is how the pore's basal Si surface may influence the magnitude of F as compared to a freestanding nanopore.)

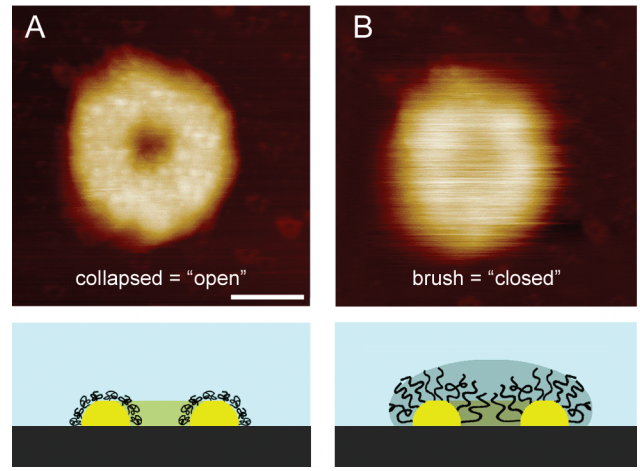

Figure 5. Reversible collapse of the PEG brush by changing solvent conditions. (A) Compact clusters of pinned micelles appear as bright spots on the ring surface after an addition of 10% 2-propanol, which is a poor solvent for PEG. Note that the collapsed state effectively opens the pore. This situation is illustrated in the accompanying schematic. (B) Collapsed PEG chains are reversibly extended into a brush by replacing the modified solution with fresh buffer. The gray shaded area in the accompanying schematic demarcates the range of the PEG brush barrier that extends beyond the periphery of the Au nanoring. Scale bar, 100 nm.

Further interesting parallels may be drawn from evidence suggesting that macromolecular transport is selectively regulated by a (bio)polymer brush formed by several natively unfolded protein domains (*i.e.*, phenylalanine-glycine (FG) domains)[45] tethered in and around biological NPCs.[21,46] Briefly, NPCs are ~50 nm pores that perforate the nuclear envelope in eukaryotic cells to form the sole transport conduits between the cytoplasm and the nucleus.[47] While small molecules (*e.g.*, water and ions) can diffuse freely through the NPC, the FG domains are disputed to collectively impose a physical barrier in the form of either a polymer brush[21,46] or a bulk-like hydrogel[48] (or both)[49] that impedes the passage of nonspecific macromolecules through the NPC. In this manner, macromolecular transport is limited to cargo-carrying transport receptors (*i.e.*, karyopherins), which exhibit biochemical interactions with the FG domains.[20] Taken in the context of nanofluidic phenomena,[26] we hypothesize that an understated characteristic of the NPC lies in its apparent lack of clogging *in vivo* despite being surrounded by a highly complex biomolecular environment. This is in marked contrast to synthetic nanopores and nanofiltra-

tion membranes, which are prone to performance deterioration (*e.g.*, reduction in membrane flux) due to nonspecific clogging effects.[26−28] Hence, a corollary to the polymer brush model of the FG domains is that it not only prevents the entry of nonspecific macromolecules into the NPC but also acts as a steric barrier that *repels* nonspecific macromolecules to minimize clogging/fouling at the NPC periphery.

Another aspect concerns molecular gating, which occurs when tethered polymers undergo conformational transitions (*e.g.*, pH, temperature, *etc.*) to modify the effective porosity of membranes.[9−14] In addition to controlling liquid permeation rates,[9−12] the reversible collapse we observe indicates that polymer brush gating may impart a valve-like mechanism to regulate the traffic of solutes. This recalls similar observations that have been made with respect to how poor solvents (*e.g.*, hexanediol) can trigger the nonphysiological (*i.e.*, no relevance to biological function) opening and closing of the NPCs[50−52] *via* a reversible collapse of the FG domains.[21] Given the appropriate stimulus,[9−12,24,25] polymer brush-gated pores can switch between a nonfouling sieve for small molecules (*e.g.*, solvent) and an open valve in their collapsed state to promote macromolecular access (*e.g.*, solute).

On a more general note, interfacial processes are often mediated by the presence of a liquid or soft complex material (*e.g.*, polymers) that protrude from the interacting surfaces. Hence, nanofabricated structures provide a useful means for studying mesoscopic, nanoscale surface-interface phenomena of both synthetic polymers[17−19,22,23] and biopolymers.[20,21] As our work shows, the use of nanofabrication can be broadly applied to investigations requiring morphological control of functional nanostructures with realistic topographies.

CONCLUSION

The objective of this work has been to scrutinize the interaction forces and morphological changes of a polymer brush-gated nanopore from the bottom-up. This was carried out by grafting PEG chains to Au nanorings constructed using nanofabrication techniques. In a good solvent (PBS buffer), the PEG chains form a polymer brush, which exhibits an exponentially decaying steric repulsive force (*i.e.*, barrier) that envelops the entire nanoring. This is further confirmed by the reversible collapse of the PEG chains by exchanging between poor and good solvent conditions. As a complement to transport studies using nanopores (which typically lack a local measure of polymeric behavior),[13,14] a deeper understanding of how polymers behave at a nanopore may be able to contribute toward more rational membrane designs. Although requiring validation in a legitimate transport context (*i.e.*, using freestanding nanopores), our results highlight possible functionalities in which polymer brushes can form a nonfouling gate- or valve-like mechanism in nanopores with relevance to both synthetic and biological nanopores.

METHODS

Fabrication of Au Nanorings. Arrays consisting of 20 × 20 submicrometer sized ring patterns were generated by electron-beam lithography. A 350 nm thick single layer of 950 kDa molecular weight polymethylmethacrylate (PMMA) was spin-coated onto p-type Si wafers passivated with a 500 nm thick thermal oxide layer. The PMMA resist was baked at 170 °C for 15 min. Designed patterns were exposed at a dose of 800 uC/cm^2 by using an electron beam with acceleration voltage of 100 kV and beam current of 20 pA. The exposed samples were developed in 3:1 isopropanol (IPA)/methyl isobutyl ketone (MIBK) for 70 s and rinsed in IPA and DI water for 20 s, respectively. About 5 nm Cr was deposited followed by ~30 nm Au on top of the patterned substrates by thermal evaporation. The lift-off process was carried out by soaking in acetone for 10 min. The samples were then rinsed with acetone, IPA, and deionized water and blown dry with nitrogen gas.

Sample Preparation. Au-patterned Si wafers were cleaned by immersion in acetone, followed by IPA, and dried under N_2. The Au-patterned Si wafers were then UV cleaned for 45 min (UVO-Cleaner Model 42-220, Jelight Company, Inc., Irvine, CA), followed by soaking in ethanol for another 30 min and dried under N_2. The Au nanorings were functionalized by immersing the clean Si wafers in 1× PBS pH 7.2 solution (GIBCO; formulated with 1.54, 155.17, and 2.71 mM of KH_2PO_4, NaCl, and Na_2HPO_4-$7H_2O$, respectively; specifications obtained from www.invitrogen.com) containing 2 mM mPEG-SH at room temperature overnight. The samples were then rinsed in copious amounts of deionized water and used immediately. The hydrodynamic diameter of the 20 kDa mPEG-SH (Nektar Pharmaceuticals) was determined by dynamic light scattering (Zetasizer Nano ZS, Malvern Instruments) conducted at room temperature in 1× PBS pH 7.2 (GIBCO; same formulation as above) containing 0.1 mM mPEG-SH. An additional 0.25 mM tris(2-carboxyethyl)phosphine (TCEP; Sigma-Aldrich) was included in this solution to prevent the formation of disulfide bonds between the mPEG-SH chains during the measurements. The light scattering data were analyzed using the Dispersion Technology Software (version 5.0) provided by Malvern Instruments. Here, the polydispersity index (PDI) given is a measure of the size ranges present in the solution (not to be confused with the PDI used in polymerization, *i.e.*, M_w/M_n). The PDI scale ranges from 0 to 1, with a value below 0.1 representing a reasonable narrow monomodal distribution. The software calculates the PDI value from the G1 correlation function and from parameters defined in the ISO standard document 13321:1996 E. Please refer to the Zetasizer Nano Series User Manual for details (www.malvern.com).

AFM Imaging and Force Volume Spectroscopy. AFM contact mode imaging and force spectroscopy measurements were carried out in 1× PBS pH 7.2 (GIBCO; same formulation as above) at room temperature using a Multimode-Nanoscope IIIA controller (Veeco, Santa Barbara, CA) equipped with a 120 μm J-scanner and a standard liquid cell. The AFM contact mode images shown in Figures 4 and 5 were obtained at a scan rate of 3.05 μm/s.

Force data were obtained as force−volume (FV) maps consisting of 32 × 32 pixels. Each pixel consists of a deflection *versus* piezo displacement (*Z*) measurement (4096 data points) obtained at an approach velocity of ~1.68 μm/s. A maximum trigger value of ~0.5 nN was imposed on every force measurement (pixel) so as to avoid damaging the tip/sample due to excess loading. The FV data were collected and analyzed by an external PC running a customized Labview application using a data acquisition card (NI6052E, National Instruments, Austin, TX). To convert the deflection into *F*, the force acting on the tip is given by the linear relation between the cantilever deflection and *Z* (when the tip is in hardwall repulsion) multiplied by the

cantilever spring constant k_c. For the force curves shown in Figure 3A, the *F versus Z* data were converted to *F versus* tip−sample approach distance (*D*) by further subtraction of the cantilever deflection from *Z*.[16] To generate stiffness maps within Labview, the application calculates from each (raw) *F versus Z* measurement (pixel) a force gradient (Δforce/ΔZ) within a range that is defined by two force values. For the stiffness map shown in Figure 3C, these values were chosen as 0.05 and 0.15 nN as they correspond to the approximate lower and upper bounds of the steric repulsion observed. It should be stressed that the stiffness maps are used in a purely qualitative sense here (*i.e.*, *relative* stiffness) given that the exponential behavior of steric repulsion is being approximated by a linear fit force gradient.

Prior to each experiment, the system was allowed to thermally equilibrate for at least 1 h. Rectangular-shaped Si_3N_4 cantilevers with V-shaped tips were used in all measurements (Biolever, Olympus/OBL, Veeco). Spring constant calibrations typically fell within a 20% margin of error from the nominal spring constant of 0.005 N/m. All tips were cleaned in oxygen plasma before use. The radius of curvature of each tip (R_{tip}) was evaluated using scanning electron microscopy (SEM) after each experiment. This is to avoid possible carbonaceous contamination of the AFM tip during SEM. Being a common problem in AFM, it is uncertain if R_{tip} is the same before and after experimentation or is blunted by the end of the experiment. All AFM data shown in this paper were obtained using a cantilever of spring constant, $k_C \approx 0.006$ N/m and a single tip with $R_{tip} = 16.1 \pm 2.4$ nm. R_{tip} (average $\pm$ standard deviation) was calculated by fitting several circles into the semihemispherical tip-end and averaging over their radii.

Acknowledgment. The authors' acknowledge the SERC Nano-Fabrication and Characterisation Facility (SNFC) at the Institute of Materials Research and Engineering for the usage of equipment and facilities. We would like to thank L. Kapinos for help with the dynamic light scattering measurements. This work is supported by the National Center of Competence in Research "Nanoscale Science" (NCCR-Nano), the Swiss National Science Foundation, the M.E. Müller Foundation of Switzerland, and the Canton Basel-Stadt.

Supporting Information Available: Formulation of the steric repulsive force due to the compression of a polymer brush by an AFM tip (based on the Alexander−de Gennes theory). This material is available free of charge *via* the Internet at http://pubs.acs.org.

REFERENCES AND NOTES

1. Granick, S.; Kumar, S. K.; Amis, E. J.; Antonietti, M.; Balazs, A. C.; Chakraborty, A. K.; Grest, G. S.; Hawker, C.; Janmey, P.; Kramer, E. J.; *et al.* Macromolecules at Surfaces: Research Challenges and Opportunities from Tribology to Biology. *J. Polym. Sci., Part B: Polym. Phys.* **2003**, *41*, 2755–2793.
2. Langer, R. Drug Delivery and Targeting. *Nature* **1998**, *392*, 5–10.
3. Bazile, D.; Prudhomme, C.; Bassoullet, M. T.; Marlard, M.; Spenlehauer, G.; Veillard, M. Stealth Me.PEG-PLA Nanoparticles Avoid Uptake by the Mononuclear Phagocytes System. *J. Pharm. Sci.* **1995**, *84*, 493–498.
4. Harris, J. M.; Chess, R. B. Effect of Pegylation on Pharmaceuticals. *Nat. Rev. Drug Discovery* **2003**, *2*, 214–221.
5. Elbert, D. L.; Hubbell, J. A. Surface Treatments of Polymers for Biocompatibility. *Annu. Rev. Mater. Sci.* **1996**, *26*, 365–394.
6. Harris, J. M. *Poly(ethylene glycol) Chemistry: Biotechnical and Biomedical Applications*; Springer: Berlin, 1992.
7. Leckband, D.; Sheth, S.; Halperin, A. Grafted Poly(ethylene oxide) Brushes as Nonfouling Surface Coatings. *J. Biomater. Sci., Polym. Ed.* **1999**, *10*, 1125–1147.
8. Shannon, M. A.; Bohn, P. W.; Elimelech, M.; Georgiadis, J. G.; Marinas, B. J.; Mayes, A. M. Science and Technology for Water Purification in the Coming Decades. *Nature* **2008**, *452*, 301–310.
9. Ito, Y.; Ochiai, Y.; Park, Y. S.; Imanishi, Y. pH-Sensitive Gating by Conformational Change of a Polypeptide Brush Grafted onto a Porous Polymer Membrane. *J. Am. Chem. Soc.* **1997**, *119*, 1619–1623.
10. Ito, Y.; Park, Y. S.; Imanishi, Y. Nanometer-Sized Channel Gating by a Self-Assembled Polypeptide Brush. *Langmuir* **2000**, *16*, 5376–5381.
11. Iwata, H.; Hirata, I.; Ikada, Y. Atomic Force Microscopic Analysis of a Porous Membrane with pH-Sensitive Molecular Valves. *Macromolecules* **1998**, *31*, 3671–3678.
12. Mika, A. M.; Childs, R. F.; Dickson, J. M. Chemical Valves Based on Poly(4-vinylpyridine)-Filled Microporous Membranes. *J. Membr. Sci.* **1999**, *153*, 45–56.
13. Caspi, Y.; Zbaida, D.; Cohen, H.; Elbaum, M. Synthetic Mimic of Selective Transport through the Nuclear Pore Complex. *Nano Lett.* **2008**, *8*, 3728–3734.
14. Jovanovic-Talisman, T.; Tetenbaum-Novatt, J.; McKenney, A. S.; Zilman, A.; Peters, R.; Rout, M. P.; Chait, B. T. Artificial Nanopores That Mimic the Transport Selectivity of the Nuclear Pore Complex. *Nature* **2009**, *457*, 1023–1027.
15. Israelachvili, J. N. *Intermolecular and Surface Forces*, 2nd ed.; Academic Press: London, 1995.
16. Butt, H. J.; Cappella, B.; Kappl, M. Force Measurements with the Atomic Force Microscope: Technique, Interpretation and Applications. *Surf. Sci. Rep.* **2005**, *59*, 1–152.
17. Ducker, R.; Garcia, A.; Zhang, J. M.; Chen, T.; Zauscher, S. Polymeric and Biomacromolecular Brush Nanostructures: Progress in Synthesis, Patterning and Characterization. *Soft Matter* **2008**, *4*, 1774–1786.
18. Jonas, A. M.; Hu, Z. J.; Glinel, K.; Huck, W. T. S. Effect of Nanoconfinement on the Collapse Transition of Responsive Polymer Brushes. *Nano Lett.* **2008**, *8*, 3819–3824.
19. Jonas, A. M.; Hu, Z. J.; Glinel, K.; Huck, W. T. S. Chain Entropy and Wetting Energy Control the Shape of Nanopatterned Polymer Brushes. *Macromolecules* **2008**, *41*, 6859–6863.
20. Lim, R. Y. H.; Fahrenkrog, B.; Koser, J.; Schwarz-Herion, K.; Deng, J.; Aebi, U. Nanomechanical Basis of Selective Gating by the Nuclear Pore Complex. *Science* **2007**, *318*, 640–643.
21. Lim, R. Y. H.; Huang, N. P.; Koser, J.; Deng, J.; Lau, K. H. A.; Schwarz-Herion, K.; Fahrenkrog, B.; Aebi, U. Flexible Phenylalanine-Glycine Nucleoporins as Entropic Barriers to Nucleocytoplasmic Transport. *Proc. Natl. Acad. Sci. U.S.A.* **2006**, *103*, 9512–9517.
22. Schmelmer, U.; Paul, A.; Kuller, A.; Steenackers, M.; Ulman, A.; Grunze, M.; Golzhauser, A.; Jordan, R. Nanostructured Polymer Brushes. *Small* **2007**, *3*, 459–465.
23. Steenackers, M.; Kueller, A.; Ballav, N.; Zharnikov, M.; Grunze, M.; Jordan, R. Morphology Control of Structured Polymer Brushes. *Small* **2007**, *3*, 1764–1773.
24. Adiga, S. P.; Brenner, D. W. Virtual Molecular Design of an Environment-Responsive Nanoporous System. *Nano Lett.* **2002**, *2*, 567–572.
25. Adiga, S. P.; Brenner, D. W. Flow Control through Polymer-Grafted Smart Nanofluidic Channels: Molecular Dynamics Simulations. *Nano Lett.* **2005**, *5*, 2509–2514.
26. Eijkel, J. C. T.; van den Berg, A. Nanofluidics: What Is It and What Can We Expect from It? *Microfluid. Nanofluid.* **2005**, *1*, 249–267.
27. Al-Amoudi, A.; Lovitt, R. W. Fouling Strategies and the Cleaning System of Nf Membranes and Factors Affecting Cleaning Efficiency. *J. Membr. Sci.* **2007**, *303*, 6–28.
28. Hong, S. K.; Elimelech, M. Chemical and Physical Aspects of Natural Organic Matter (NOM) Fouling of Nanofiltration Membranes. *J. Membr. Sci.* **1997**, *132*, 159–181.
29. Zhao, B.; Brittain, W. J. Polymer Brushes: Surface-Immobilized Macromolecules. *Prog. Polym. Sci.* **2000**, *25*, 677–710.
30. Feldman, K.; Hahner, G.; Spencer, N. D.; Harder, P.; Grunze, M. Probing Resistance to Protein Adsorption of Oligo(ethylene glycol)-Terminated Self-Assembled Monolayers by Scanning Force Microscopy. *J. Am. Chem. Soc.* **1999**, *121*, 10134–10141.

31. de Gennes, P. G. Polymers at an Interface—A Simplified View. *Adv. Colloid Interface Sci.* **1987**, *27*, 189–209.
32. de Gennes, P. G. Conformations of Polymers Attached to an Interface. *Macromolecules* **1980**, *13*, 1069–1075.
33. Alexander, S. Adsorption of Chain Molecules with a Polar Head A Scaling Description. *J. Phys.* **1977**, *38*, 983–987.
34. O'Shea, S. J.; Welland, M. E.; Rayment, T. An Atomic-Force Microscope Study of Grafted Polymers on Mica. *Langmuir* **1993**, *9*, 1826–1835.
35. Butt, H. J.; Kappl, M.; Mueller, H.; Raiteri, R.; Meyer, W.; Ruhe, J. Steric Forces Measured with the Atomic Force Microscope at Various Temperatures. *Langmuir* **1999**, *15*, 2559–2565.
36. Muller, M. T.; Yan, X. P.; Lee, S. W.; Perry, S. S.; Spencer, N. D. Lubrication Properties of a Brushlike Copolymer as a Function of the Amount of Solvent Absorbed within the Brush. *Macromolecules* **2005**, *38*, 5706–5713.
37. Koutsos, V.; vanderVegte, E. W.; Pelletier, E.; Stamouli, A.; Hadziioannou, G. Structure of Chemically End-Grafted Polymer Chains Studied by Scanning Force Microscopy in Bad-Solvent Conditions. *Macromolecules* **1997**, *30*, 4719–4726.
38. Halperin, A.; Tirrell, M.; Lodge, T. P. Tethered Chains in Polymer Microstructures. *Adv. Polym. Sci.* **1992**, *100*, 31–71.
39. Milner, S. T. Polymer Brushes. *Science* **1991**, *251*, 905–914.
40. Oesterhelt, F.; Rief, M.; Gaub, H. E. Single Molecule Force Spectroscopy by AFM Indicates Helical Structure of Poly(ethylene-glycol) in Water. *New J. Phys.* **1999**, *1*, 1.
41. Heuberger, M.; Drobek, T.; Spencer, N. D. Interaction Forces and Morphology of a Protein-Resistant Poly(ethylene glycol) Layer. *Biophys. J.* **2005**, *88*, 495–504.
42. Patra, M.; Linse, P. Reorganization of Nanopatterned Polymer Brushes by the AFM Measurement Process. *Macromolecules* **2006**, *39*, 4540–4546.
43. Koutsioubas, A. G.; Vanakaras, A. G. Polymer Brushes on Periodically Nanopatterned Surfaces. *Langmuir* **2008**, *24*, 13717–13722.
44. Asatekin, A.; Kang, S.; Elimelech, M.; Mayes, A. M. Anti-Fouling Ultrafiltration Membranes Containing Polyacrylonitrile-Graft-Poly(ethylene oxide) Comb Copolymer Additives. *J. Membr. Sci.* **2007**, *298*, 136–146.
45. Denning, D. P.; Patel, S. S.; Uversky, V.; Fink, A. L.; Rexach, M. Disorder in the Nuclear Pore Complex: The FG Repeat Regions of Nucleoporins are Natively Unfolded. *Proc. Natl. Acad. Sci. U.S.A.* **2003**, *100*, 2450–2455.
46. Miao, L. L.; Schulten, K. Transport-Related Structures and Processes of the Nuclear Pore Complex Studied through Molecular Dynamics. *Structure* **2009**, *17*, 449–459.
47. Lim, R. Y. H.; Aebi, U.; Fahrenkrog, B. Towards Reconciling Structure and Function in the Nuclear Pore Complex. *Histochem. Cell Biol.* **2008**, *129*, 105–116.
48. Frey, S.; Gorlich, D. A Saturated FG-Repeat Hydrogel Can Reproduce the Permeability Properties of Nuclear Pore Complexes. *Cell* **2007**, *130*, 512–23.
49. Patel, S. S.; Belmont, B. J.; Sante, J. M.; Rexach, M. F. Natively Unfolded Nucleoporins Gate Protein Diffusion across the Nuclear Pore Complex. *Cell* **2007**, *129*, 83–96.
50. Jaggi, R. D.; Franco-Obregon, A.; Muhlhausser, P.; Thomas, F.; Kutay, U.; Ensslin, K. Modulation of Nuclear Pore Topology by Transport Modifiers. *Biophys. J.* **2003**, *84*, 665–670.
51. Ribbeck, K.; Gorlich, D. The Permeability Barrier of Nuclear Pore Complexes Appears to Operate *via* Hydrophobic Exclusion. *EMBO J.* **2002**, *21*, 2664–2671.
52. Shulga, N.; Goldfarb, D. S. Binding Dynamics of Structural Nucleoporins Govern Nuclear Pore Complex Permeability and May Mediate Channel Gating. *Mol. Cell. Biol.* **2003**, *23*, 534–542.